



Minerva Access is the Institutional Repository of The University of Melbourne

Author/s:

Zhao, D;Pinares-Garcia, P;McKenzie, CE;Bleakley, LE;Forster, IC;Wong, VHY;Nguyen, CTO;Scheffer, IE;Reid, CA;Bui, BV

Title:

Retinal Dysfunction in a Mouse Model of HCN1 Genetic Epilepsy

Date:

2023-03-22

Citation:

Zhao, D., Pinares-Garcia, P., McKenzie, C. E., Bleakley, L. E., Forster, I. C., Wong, V. H. Y., Nguyen, C. T. O., Scheffer, I. E., Reid, C. A. & Bui, B. V. (2023). Retinal Dysfunction in a Mouse Model of HCN1 Genetic Epilepsy. *Journal of Neuroscience*, 43 (12), pp.2199-2209. <https://doi.org/10.1523/JNEUROSCI.1615-22.2022>.

Persistent Link:

<https://hdl.handle.net/11343/333643>

License:

[CC BY-NC-SA](#)

Retinal Dysfunction in a Mouse Model of HCN1 Genetic Epilepsy

Da Zhao,^{1*} Paulo Pinares-Garcia,^{2*} Chaseley E. McKenzie,² Lauren E. Bleakley,^{2*} Ian C. Forster,² Vickie H.Y. Wong,¹ Christine T.O. Nguyen,¹  Ingrid E. Scheffer,^{2,3,4,5} Christopher A. Reid,^{2,3†} and Bang V. Bui^{1†}

¹Department of Optometry and Vision Sciences, School of Health Sciences, Faculty of Medicine Dentistry and Health Sciences, University of Melbourne, Parkville 3010, Victoria, Australia, ²Early Development Division, Florey Institute of Neuroscience and Mental Health, Parkville 3010, Victoria, Australia, ³Epilepsy Research Centre, Department of Medicine, University of Melbourne/Austin Health, Heidelberg 3084, Victoria, Australia, ⁴Murdoch Children's Research Institute, The Royal Children's Hospital, Parkville 3052, VIC Australia, and ⁵Department of Paediatrics, University of Melbourne, Royal Children's Hospital, Parkville 3052, Victoria Australia

Pathogenic variants in *HCN1* are associated with a range of epilepsy syndromes including a developmental and epileptic encephalopathy. The recurrent *de novo* *HCN1* pathogenic variant (M305L) results in a cation leak, allowing the flux of excitatory ions at potentials where the wild-type channels are closed. The *Hcn1*^{M294L} mouse recapitulates patient seizure and behavioral phenotypes. As *HCN1* channels are highly expressed in rod and cone photoreceptor inner segments, where they shape the light response, mutated channels are likely to impact visual function. Electroretinogram (ERG) recordings from male and female mice *Hcn1*^{M294L} mice revealed a significant decrease in the photoreceptor sensitivity to light, as well as attenuated bipolar cell (P2) and retinal ganglion cell responses. *Hcn1*^{M294L} mice also showed attenuated ERG responses to flickering lights. ERG abnormalities are consistent with the response recorded from a single female human subject. There was no impact of the variant on the structure or expression of the *Hcn1* protein in the retina. *In silico* modeling of photoreceptors revealed that the mutated *HCN1* channel dramatically reduced light-induced hyperpolarization, resulting in more Ca²⁺ flux during the response when compared with the wild-type situation. We propose that the light-induced change in glutamate release from photoreceptors during a stimulus will be diminished, significantly blunting the dynamic range of this response. Our data highlight the importance of *HCN1* channels to retinal function and suggest that patients with *HCN1* pathogenic variants are likely to have a dramatically reduced sensitivity to light and a limited ability to process temporal information.

Key words: electroretinography; epilepsy; *HCN1*; photoreceptors; retina

Significance Statement

Pathogenic variants in *HCN1* are emerging as an important cause of catastrophic epilepsy. *HCN1* channels are ubiquitously expressed throughout the body, including the retina. Electroretinogram recordings from a mouse model of *HCN1* genetic epilepsy showed a marked decrease in the photoreceptor sensitivity to light and a reduced ability to respond to high rates of light flicker. No morphologic deficits were noted. Simulation data suggest that the mutated *HCN1* channel blunts light-induced hyperpolarization and consequently limits the dynamic range of this response. Our results provide insights into the role *HCN1* channels play in retinal function as well as highlighting the need to consider retinal dysfunction in disease caused by *HCN1* variants. The characteristic changes in the electroretinogram open the possibility of using this tool as a biomarker for this *HCN1* epilepsy variant and to facilitate development of treatments.

Received Aug. 25, 2022; revised Dec. 6, 2022; accepted Dec. 9, 2022.

Author contributions: D.Z., L.E.B., I.C.F., V.H.Y.W., C.T.O.N., C.A.R., and B.V.B. designed research; D.Z., P.P.-G., C.E.M., I.C.F., I.E.S., and B.V.B. performed research; D.Z., P.P.-G., I.C.F., C.A.R., and B.V.B. analyzed data; B.V.B. wrote the paper.

This research was supported by National Health and Medical Research Council (NHMRC) Program Grant 10915693 to C.A.R. and I.E.S. I.E.S. is also the recipient of NHMRC Practitioner Fellowship 1104831 and Investigator Grant 1172897. This work was made possible through the Victorian State Government Operational Infrastructure Support and Australian Government NHMRC Independent Research Institute Infrastructure Support Scheme. We thank the patient and her family for participating in our research.

*D.Z., P.P.-G., and L.E.B. are joint first authors.

†C.A.R. and B.V.B. are joint senior authors.

The authors declare no competing financial interests.

Correspondence should be addressed to Bang V. Bui at bvb@unimelb.edu.au.

<https://doi.org/10.1523/JNEUROSCI.1615-22.2022>

Copyright © 2023 the authors

Introduction

Hyperpolarization-activated cyclic nucleotide-gated (HCN) channels are found in the heart, and in the CNS and peripheral nervous system. *HCN1-4* encode four HCN channel subtypes (Biel et al., 2009), which control neuronal activity through a variety of mechanisms that include the modulation of rhythmic activity, dendritic integration, transmission of synaptic responses, and synaptic plasticity (Biel et al., 2009). Pathogenic variation in *HCN1* has emerged as an important cause of epilepsy (Nava et al., 2014; Bonzanni et al., 2018; Marini et al., 2018; Porro et al., 2021). *De novo* *HCN1* pathogenic variants typically cause developmental

and epileptic encephalopathies (DEEs), the most severe group of epilepsies characterized by drug-resistant seizures and developmental impairment (Nava et al., 2014; Marini et al., 2018). Despite their localization throughout the CNS and peripheral nervous system (Moosmang et al., 2001), little is known about sensory deficits associated with *HCN1* pathogenic variants.

Recently, we reported a child with *HCN1* DEE who had difficulty discriminating colors (McKenzie et al., 2022). Although all four HCN channel isoforms/subtypes are expressed in the retina, HCN1 is the most widely expressed isoform being localized to rod and cone inner segments (Moosmang et al., 2001; Demontis et al., 2002). Rod photoreceptors (Phs) express only HCN1 (Moosmang et al., 2001; Müller et al., 2003), whereas cone photoreceptors also express HCN2 and HCN3, although at lower levels (Müller et al., 2003). Additionally, HCN1 channels are found on cone bipolar cells (Müller et al., 2003) as well as amacrine and retinal ganglion cells (Müller et al., 2003).

HCN1 channels have an established role in photoreceptors, generating the hyperpolarization-activated cation current I_h (Moosmang et al., 2001; Demontis et al., 2002; Knop et al., 2008; Tanimoto et al., 2012). HCN1 channels are activated during hyperpolarization in bright light and depolarize the cell toward the dark membrane potential (V_m), making the light response more transient (Baylor et al., 1984; Hestrin, 1987; Barrow and Wu, 2009). Their slow activation plays a role in defining the photoreceptor membrane potential and therefore the activity of other voltage sensitive channels (Della Santina et al., 2012). HCN1 channels may also modulate bipolar cell synaptic transmission (Chevalyere and Castillo, 2002; Müller et al., 2003; Della Santina et al., 2010), particularly those bipolar cells that show high temporal tuning (Euler et al., 2014) and contribute to motion detection (Yonehara et al., 2013). Thus, response shaping throughout the retina by HCN1 channels has a role in facilitating temporal resolution of visual stimuli. In line with a role for HCN1 in retinal function, genetic deletion of *Hcn1* in mice results in prolongation of the scotopic and photopic electroretinogram (ERG) responses (Seeliger et al., 2011; Sothilingam et al., 2016). At mesopic light levels, rod HCN1 channels shape the temporal characteristics of cone responses (Lankford et al., 2022). Moreover, deletion of *Hcn1* results in a reduction of the dynamic range, with saturation of the downstream retinal network during bright light stimulation (Knop et al., 2008; Seeliger et al., 2011; Sothilingam et al., 2016). Whether retinal dysfunction also occurs in patients carrying *HCN1* pathogenic variants remains unclear.

Here we investigated the impact of an *HCN1* pathogenic variant on phototransduction and downstream retinal processing, including temporal resolving capacity using ERG on the *Hcn1*^{M294L} mouse model of DEE. The *Hcn1*^{M294L} mouse carries the homolog of the *de novo* *HCN1* M305L variant identified in two unrelated patients with DEEs (Marini et al., 2018; Bleakley et al., 2021). The *Hcn1*^{M294L} mouse recapitulates many of the features of the human disease, including spontaneous seizures, hyperactivity, and cognitive impairment (Bleakley et al., 2021). This mutation, located in the S5 transmembrane domain, disrupts the voltage dependence, rendering the HCN1 channel constitutively open and resulting in aberrant cation “leak” (Marini et al., 2018; Bleakley et al., 2021; Hung et al., 2021). Neuronal depolarization caused by the cation leak is proposed to underlie excitability leading to seizures (Bleakley et al., 2021).

Materials and Methods

Ethics and animal welfare

Experiments were performed in accordance with the Prevention of Cruelty to Animals Act, 1986, under the guidelines of the National

Health and Medical Research Council (NHMRC) of Australia *Code of Practice for the Care and Use of Animals for Experimental Purposes*. All experiments were approved by the Animal Ethics Committee at the Florey Institute of Neuroscience and Mental Health before commencement. Animals were monitored in line with protocols approved by this committee. Anesthesia and analgesia were used where appropriate. Mice were acclimatized to experimental rooms for at least 30 min before experimentation. At the conclusion of experimentation, mice were killed by cervical dislocation or decapitation following deep anesthesia.

Human procedures and ethics

The parents of the patient provided written informed consent for research participation. The research was approved by the Human Research Ethics Committee of Austin Health (H2007/02,961). Electroretinogram recordings were made from a patient carrying the *HCN1*^{M305L} variant, with pupil dilation measured using lower eye lid electrodes with skin electrodes (Kriss and Russell-Eggitt, 1992). With the room lights on, a Ganzfeld stimulator (ColorDome, Diagnosys) was used to generate a single moderate-intensity flash (~5 cd.s/m²) to produce a photopic cone ERG followed by a 30 Hz flicker stimulus of the same intensity.

Generation of the *Hcn1*^{M294L} mouse model

A guide RNA target site close to amino acid 294 of the mouse *Hcn1* gene was identified using the UCSC Genome Browser [<https://genome.ucsc.edu/> (accessed June 22, 2021)]. The guide RNA sequence used was 5'-GAAGCAGCATCATGCCAATG-3'. CRISPR RNA (crRNA; Integrated DNA Technologies) was annealed with transactivating crRNA (tracrRNA) to form a functional crRNA:tracrRNA guide RNA duplex. Cas9 nuclease (Integrated DNA Technologies) was incubated with the guide RNAs to form a ribonucleoprotein (RNP) complex. A single-stranded repair oligo containing the desired amino acid change (Integrated DNA Technologies) was used as a repair template. The C147-HCN1-M294L repair template sequence was 5'-TGCTGACAGATATCCACATGACCTATGACCTC GCCAGTGCTGTGGTGAGGATCTTCAACCTCATCGGAATGTTGCT-GCTTCTGTGCCACTGGGATGGTGTCTTTCAGTTCCTGGTTCCCC-TGCTGCAGGACTTCCCA-3'. Cas9 nuclease (30 ng/μl), the RNPs (30 ng/μl) and the single-stranded DNA homology-directed repair template (30 ng/μl) were microinjected into the pronucleus of C57BL/6J zygotes at the pronuclei stage. Injected zygotes were transferred into the uterus of pseudopregnant F1 females.

Animal housing and husbandry

Mice were bred on site at the Florey Institute of Neuroscience and Mental Health. Male heterozygous *Hcn1*^{M294L} mice were mated with wild-type C57BL/6J female mice, yielding either *Hcn1*^{+/+} [wild-type (WT)] or *Hcn1*^{M294L/+} offspring. Mice were housed in standard rodent cages with access to dry pellet food and water *ad libitum*. Room lighting was maintained at <50 lux with a 12 h dark/light cycle (lights on at 8:00 A.M.) to minimize the potential for light-induced retinal injury. For all experiments, both male and female mice were used, with littermates used wherever possible.

General procedures

Ten *Hcn1*^{M294L} mice and 10 *Hcn1*^{WT} mice were used. Animals underwent noninvasive assessment of retinal structure and function. Before the procedure, animals were dark adapted overnight, then weighed and anesthetized with an intraperitoneal injection of ketamine (80 mg/kg) and xylazine (10 mg/kg; Troy Laboratory). The mixture was diluted in sterile injectable saline (1:10) to aid with hydration and ease of administration (10 μl/g).

Topical anesthesia and pupil mydriasis were achieved with single drops of proxymetacaine 0.5% (Alcaine, Alcon) and tropicamide 0.5% (Mydriacyl, Alcon). Corneal hydration was maintained with lubricating eye drops during ERG (Celluvisc, Allergan) and imaging (Systane, Alcon). During both ERG and optical coherence tomograph (OCT) assessment, body temperature was maintained at 37°C to prevent hypothermia. At the end of *in vivo* assessment, anesthetized

animals were killed by cervical dislocation and eyes were collected for immunohistochemistry.

Electroretinography

Mice were dark adapted overnight before ERG. Experiments were conducted in a lightproof room, and all preparation was undertaken with only the aid of a dim red headlight to minimize light exposure. Following the induction of anesthesia and mydriasis, animals were lightly secured to a water-heated platform to minimize movement and breathing artifacts. Custom-made silver chloride active electrodes (A&E Metal Merchants) were placed on the apex of the corneas, with the reference ring-shaped electrode placed around the equator of the eye. A grounding needle electrode (Grass) was then inserted subcutaneously into the tail, before positioning the Ganzfeld bowl at eye level. Animals were set up in a Faraday cage to block out electromagnetic noise. Raw signals were processed via a preamplifier (model P511 AC Amplifier, Grass) and a main amplifier (model ML785 Powerlab 8SP, ADInstruments) with a bandpass filter setting of 0.1–1000 Hz. Signals were recorded using Scope software (ADInstruments) and exported for offline analysis. Analysis of line noise characteristics showed that there was no difference between the two strains (Fig. 3D inset).

Scotopic responses. Following electrode setting a further 10 min was allowed to ensure that the eyes had completely recovered from the red light used during setup. ERGs were then elicited using a range of luminous energies (from -5.53 to $2.07 \log \text{ cd.s/m}^2$, 0.1–4 ms) starting from the dimmest, where 20 responses were recorded and averaged. As the light intensity increased, the number of repeated flashes was reduced and the time between subsequent flashes was progressively lengthened to avoid adaptation. This wide range of stimuli allowed for the isolation of retinal ganglion cell-mediated responses [scotopic threshold response (STR)] at the dimmest light levels, as well as inner retinal inhibitory circuits [oscillatory potentials (OPs)], P2, and photoreceptor (P3) responses at moderate and high scotopic light levels.

Photopic responses. Following the collection of scotopic responses, animals were light adapted for 10 min to a white background of 140 cd/m^2 . Once signals had stabilized, a sequence of luminous energies ranging from 0.76 to $2.67 \log \text{ cd.s/m}^2$ elicited the cone pathway-driven a-wave, b-wave, and OPs. At each intensity, 10 signals were recorded with an interstimulus interval of 2 s. To assess both transient and sustained responses, a longer flash ($2.67 \log \text{ cd.s/m}^2$, 256 ms) was delivered.

Temporal resolution. To quantify the temporal processing capacity of the eye, we elicited responses using progressively higher temporal frequencies with a fixed light intensity ($3.99 \log \text{ cd.s/m}^2$). Flickering stimuli ranged from 5 to 45 Hz (in 5 Hz steps) with a 50% duty cycle without any background light.

Spectral response. Spectral response characteristics of the eye were assessed using responses to flicker lights (10 Hz, 50% duty cycle) of varying peak wavelength, generated by a xenon light source with a monochromator (150 W Polychrome V, Till Photonics). Wavelengths ranged from 420 to 680 nm in 20 nm steps (bandwidth, 10 nm).

Photoreceptor P3 analysis. As previously described (Bui et al., 2005), to analyze the scotopic photoreceptor response (P3), the first corneal electronegative component of the ERG waveform (the a-wave) was modeled as a function of time (in milliseconds) and intensity (in $\log \text{ cd.s/m}^2$) using a delayed Gaussian function (Eq. 1; Lamb and Pugh, 1992) to quantify the amplitude (i.e., number of receptors and their outer segment length (Rm_{P3} ; in microvolts) and the sensitivity [amplification of the phototransduction cascade (S); in $\text{cd}^{-1} \cdot \text{m}^2/\text{s}^3$]. The delay term (t_d ; in seconds) describes both biochemical and other recording latencies. The model was fit to the two brightest intensities (1.55 and $2.07 \log \text{ cd.s/m}^2$), which elicit photoreceptor (a-wave) responses of saturated amplitude and free of b-wave intrusion. The model was optimized by changing all parameters to minimize the root mean square (rms) error term (Solver module in Excel, Microsoft). The photopic a-wave was modeled using the same equation fit as an ensemble to the brightest three light levels (2.07 , 2.37 , and $2.67 \log \text{ cd.s/m}^2$), as follows:

$$P3(i, t) = Rm_{P3} \cdot \left[1 - e^{-i \cdot \int S \cdot (t - t_d)^2} \right] \text{ for } t > t_d. \quad (1)$$

Bipolar cell P2 and amacrine cell oscillatory potential analysis. For both scotopic and photopic waveforms, the bipolar cell-dominated P2 component of the ERG was quantified by first subtracting the family of P3 responses from their respective intensities of the raw ERG waveform. The derived waveform contains the underlying P2 and the OPs. The OPs provide information about inner retinal inhibitory pathways involving amacrine cells (Wachtmeister, 1998). The OPs and P2 were isolated by bandpass (-3 dB at 50 and 280 Hz) and low-pass filtering (-3 dB at 50 Hz), respectively. OPs were then quantified by the amplitude from baseline of their peak response at the brightest light level (scotopic, $2.07 \log \text{ cd.s/m}^2$; photopic, $2.67 \log \text{ cd.s/m}^2$).

The response amplitude ($P2_{\text{max}}$; in microvolts) and sensitivity ($1/K$, $\log \text{ cd.s/m}^2$) of bipolar cells was then quantified by fitting the P2 amplitude as a function of all stimulus intensities (i ; $\log \text{ cd.s/m}^2$) using a saturating hyperbolic function (Eq. 2). The function was fit to the range of either scotopic or photopic responses by minimizing the rms error term (Excel), as follows:

$$P2(i) = P2_{\text{max}} \cdot \frac{i}{i + K}. \quad (2)$$

Ganglion cell scotopic threshold response. Ganglion cell responses are known to dominate the rodent ERG waveform at light levels near absolute threshold (Saszik et al., 2002; Bui and Fortune, 2004). The amplitude of the positive lobe of the STR (pSTR) was taken at -5.01 and $-4.90 \log \text{ cd.s/m}^2$.

Optical coherence tomography

Following ERG recordings, animals underwent *in vivo* retinal structure imaging using spectral-domain OCT (Spectralis SD-OCT2, Heidelberg Engineering). A drop of ocular lubricant gel (Gentel Tears, Alcon) and a coverslip were used to rehydrate and remove any opacities that developed from general anesthesia used during ERG recordings. Once clear optics were achieved (10–15 min), excess eye gel was removed, and a single drop of eye lubricant (Systane, Alcon) was applied to improve tear film optics for OCT imaging. The center of cornea was aligned to the lens of OCT via a three-dimensional adjustable platform. Images were acquired with a volumetric scan pattern ($7.6 \times 6.3 \times 1.9 \text{ mm}$) centered over the optic nerve head. Each volume scan consisted of 121 vertical B-scans (five repeats), and each B-scan was made up of 768 A-scans ($3.87 \mu\text{m}$ axial, $9.8 \mu\text{m}$ lateral resolution).

Analysis used the automated segmentation algorithm of the manufacturer software (HEYEX, Heidelberg Engineering), which was checked for errors. Thicknesses were averaged across an annulus from 3 to 6 mm (i.e., Early Treatment Diabetic Retinopathy Study outer ring) for the retinal nerve fiber layer (RNFL), ganglion cell inner plexiform layer (IPL), inner nuclear layer (INL), outer plexiform layer (OPL), outer nuclear layer (ONL), photoreceptor (Ph), as well as total retinal thickness (TRT).

Immunohistochemistry

Following *in vivo* assessment, animals were killed, and eyes were enucleated and immersion fixed in 4% paraformaldehyde prepared in 0.1 M PBS, pH 7.4, for 15 min at room temperature, and cryoprotected in 30% sucrose at 4°C overnight. Eyes were then embedded in Tissue-Tek O.C.T. Compound (Miles), and frozen at -20°C . Serial sections (thickness, $14 \mu\text{m}$) were collected on Superfrost Plus slides. For immunostaining, sections were permeabilized in PBS containing 0.1% Triton X-100 for 10 min, followed by 1 h incubation in CAS-Block (catalog #008120, Thermo Fisher Scientific) to block nonspecific labeling. Sections were incubated O/N at 4°C with polyclonal rabbit anti-HCN1 (1 : 100; catalog #APC-056 Alomone Labs), washed (0.1 M PBS, $3 \times 5 \text{ min}$) and incubated with secondary antibody conjugated to Alexa Fluor-488 for 2 h at room temperature (1 : 500; Thermo Fisher Scientific). Sections were visualized with a confocal microscope (model LSM780, Zeiss), and image files were processed with Zen Blue software (Carl Zeiss).

Table 1. Modeling parameters

Current	G_{\max} (nS)	E_r (mV)	Kinetic parameters*	Model type	Reference
I_l	0.52	−74	N/A	Ohmic	Liu and Kourennyi (2004)
I_{Kx}	1.04	−74	$\alpha_{0.5,Kx} = \text{ms}^{-1}$ $\beta_{0.5,Kx} = 6.6 \cdot 10^{-4} \text{ms}^{-1}$ $S_{Kx} = 5.7 \text{ mV}$ $V_{0.5,Kx} = -50 \text{ mV}$	Activation 2 state	Liu and Kourennyi (2004)
I_{Ca}	4	40	$\alpha_{0.5,Ca} = 0.1 \text{ ms}^{-1}$ $V_{0.5,mCa} = -10 \text{ mV}$ $S_{m,Ca} = 6 \text{ mV}$ $\gamma_{0.5,Ca} = 0.01 \text{ ms}^{-1}$ $\delta_{0.5,Ca} = 5.0 \cdot 10^{-4} \text{ms}^{-1}$ $V_{0.5,Ca} = 11 \text{ mV}$ $S_{h,Ca} = 9 \text{ mV}$	Activation 2 state Inactivation 2 state	Liu and Kourennyi (2004)
I_h	3	−32	$\alpha = 0.002 \text{ ms}^{-1}$ $\beta = 0.250 \text{ ms}^{-1}$ $\gamma = 0.03 \text{ ms}^{-1}$ $\delta = 0.01 \text{ ms}^{-1}$ $z_{\alpha\beta} = 0.7$ $z_{\gamma\delta} = 0.2$ $ff = 3$	WT: 10 state allosteric M294L: 4 state allosteric	Hung, Forster et al. (2021)

N/A, Not applicable.

*Symbols for rate constants correspond to those used in cited references.

Photoreceptor modeling and simulations

A passive electrical model (Table 1) for a single photoreceptor cell was based on previously published models comprising parallel conductances, membrane capacitance, and photocurrent source (Kamiyama et al., 1996; Liu and Kourennyi, 2004; Publio et al., 2006). Current through each conductance was defined by Equation 3, as follows:

$$I = G^{\max} P_{\text{open}} (V_m - E_r). \quad (3)$$

In Equation 3, G^{\max} is the maximum conductance, P_{open} the open probability, and E_r is the reversal potential. The following conductances were incorporated into the model cell: leak conductance (G_l); nonactivating K current (G_{Kx}); hyperpolarization-activated conductance (G_h), and L-type calcium conductance (G_{Ca}). The conductance models for G_l , G_{Kx} , and G_{Ca} and associated parameters (rate constants, reversal potential, and maximum conductance) were the same as used in the study by Liu and Kourennyi (2004; Table 1). The photoreceptor cell capacitance was defined as 30 pF, and the photocurrent stimulus (I_{photo}) in response to a bright flash used previously published parameters (Liu and Kourennyi, 2004). To model G_h corresponding to Hcn1^{WT} channels, a 10-state allosteric model was used as previously described by Hung et al. (2021) to predict P_{open} . This model was originally used to describe Hcn1^{WT} currents in *Xenopus* oocytes, and the kinetic parameters were adjusted to take account of the faster kinetics in the mouse brain (34–35°C). Only the rate constants were altered to give an acceptable match to previously published voltage-clamp recordings from layer 5 pyramidal neurons (Bleakley et al., 2021, their Fig. 5; Table 1). To model G_h corresponding to the Hcn1^{M294L} channel, the four-state allosteric model was used (Hung et al., 2021) with the same rates for activation and channel opening as for the WT (Table 1) as this model best described the measured I_h in layer 5 pyramidal neurons. To predict the time course of V_m and the corresponding current components in response to a simulated light flash were given by solving for V_m in Equation 4, using Berkeley Madonna (version 8.3.9), as follows:

$$C_m \frac{dV_m}{dt} = -(I_{Kx} + I_h + I_{Ca} + I_l + I_{\text{photo}}), \quad (4)$$

where the subscripts indicate each current component, as defined above.

Statistical analysis

All statistical analyses were performed using Prism software (version 9; GraphPad Software). Data are reported and plotted as the mean \pm SEM.

Other data were first analyzed using a Shapiro–Wilk test for normality. Statistical significance was then determined using a two-tailed Student's t test (paired or unpaired, as appropriate) for normally distributed data, or a Mann–Whitney U test for non-normally distributed data. For parameters collected across a range of stimulus conditions a two-way repeated-measures (RM) ANOVA was used to compare the two mouse strains, with Sidak *post hoc* test used at specific stimulus conditions. Statistical significance was set at $p < 0.05$.

Results

Retinal function and structure in Hcn1^{M294L} mice

Figure 1A shows the average scotopic ERG waveform at selected intensities in both Hcn1^{WT} and Hcn1^{M294L} mice. At the brightest intensity (2.07 log cd.s/m²), there was a small deficit in the photoreceptor a-wave, with moderate intensities highlighting a bipolar cell b-wave attenuation (−2.75 log cd.s/m²). At the dimmest light levels, the ganglion cell pSTR was also reduced in size (−5.01 and −4.90 log cd.s/m²). Modeling of the a-wave leading edge revealed no difference in phototransduction amplitude (Fig. 1B; $t_{(14)} = 1.39$, $p = 0.19$, t test) but significantly reduced sensitivity to light (Fig. 1C; $t_{(14)} = 2.67$, $p = 0.018$, t test) in Hcn1^{M294L} mice compared with their WT counterparts. Downstream of photoreceptors, rod bipolar cell responses were both significantly reduced in amplitude (Fig. 1D; $t_{(14)} = 3.78$, $p = 0.002$, t test) and less sensitive to light (Fig. 1E; $t_{(14)} = 4.86$, $p = 0.0003$, t test). Additionally, scotopic ganglion cell pSTRs (Fig. 1F; $t_{(14)} = 4.80$, $p = 0.0003$, t test) were significantly reduced, whereas amacrine cell OPs were not affected (Fig. 1G; $t_{(14)} = 0.65$, $p = 0.53$, t test).

Hcn1^{M294L} mice that showed photopic ERG responses elicited with short flashes on a bright-light background, have a smaller b-wave that was less sustained than Hcn1^{WT} mice (Fig. 1H). This effect is readily appreciated with the longer flash, whereby Hcn1^{M294L} mice also showed a transient component but only a very small, sustained b-wave tail. Modeling the photopic a-wave (Fig. 1H, inset) showed that cone photoreceptors in Hcn1^{M294L} mice produced response amplitudes similar to those in Hcn1^{WT} controls (Fig. 1I; $t_{(14)} = 0.69$, $p = 0.49$, t test), but were significantly less sensitive to light (Fig. 1J; $t_{(14)} = 3.29$, $p = 0.005$, t test). These photoreceptor deficits resulted in similar cone bipolar cell response amplitudes (Fig. 1K; $t_{(14)} = 1.95$, $p = 0.07$, t test), which

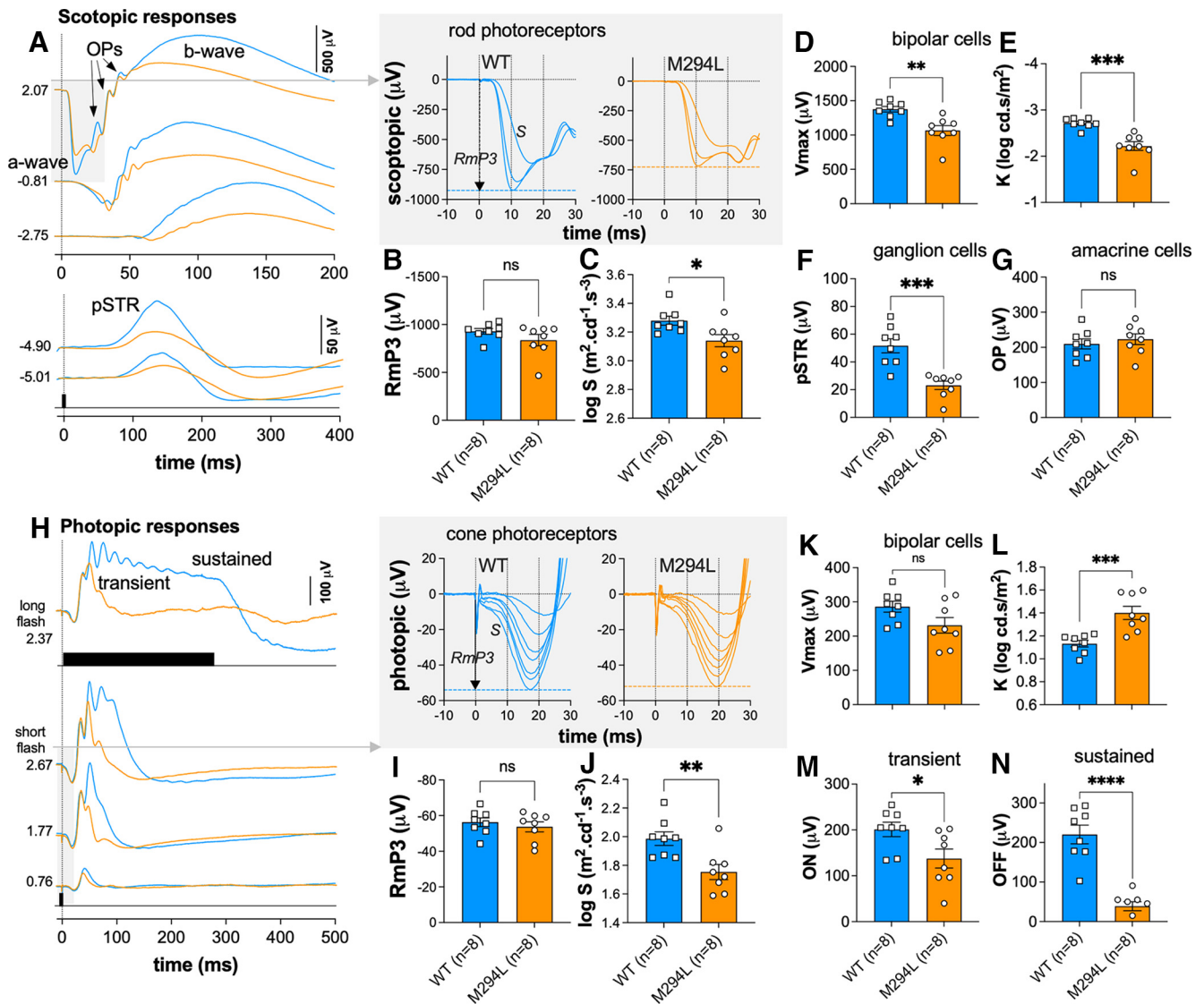


Figure 1. Deficits in scotopic and photopic electroretinogram responses in *Hcn1*^{M294L} mice. **A**, Group averaged *Hcn1*^{WT} mice (*WT*, *n* = 8, blue) and *Hcn1*^{M294L} mice (*M294L*, *n* = 8, orange) scotopic waveforms at selected light levels. Photoreceptor (a-wave), bipolar cell-mediated (b-wave) and amacrine cell (Oscillatory potential, OPs) components are analyzed at brighter light levels, whereas the ganglion cell pSTR was isolated at very dim light levels (−4.9 and −5.01 log cd.s/m²). Rod photoreceptor response were analyzed by modeling the phototransduction cascade. **B**, Group average (±SEM) scotopic phototransduction amplitude (*Rmp*₃) for *Hcn1*^{WT} (*n* = 8, blue) and *Hcn1*^{M294L} (*n* = 8, orange) mice. Individual eyes are shown. **C**, Scotopic phototransduction amplification (log *S*). **D**, Scotopic bipolar cell amplitude (*V*_{max}). **E**, Scotopic bipolar cell sensitivity (*K*). **F**, pSTR. **G**, Scotopic amacrine cell amplitude (OPs). **H**, Group-averaged photopic waveforms at selected light levels. **I**, Photopic phototransduction amplification. **J**, Photopic phototransduction amplification. **K**, Photopic bipolar cell amplitude. **L**, Photopic bipolar cell sensitivity. **M**, Amplitude of transient b-wave measured after light onset. **N**, Amplitude of sustained b-wave measured just before stimulus offset (256 ms). Additional analysis of ON and OFF components can be found in Figure 2. For all panels: ns, not significant; **p* < 0.05; ***p* < 0.01; ****p* < 0.001; *****p* < 0.0001.

were also less sensitive to light (Fig. 1L; *t*₍₁₄₎ = 4.20, *p* = 0.0009, *t* test). Analysis of the longer flash showed that both transient (Fig. 1M; *t*₍₁₄₎ = 2.45, *p* = 0.028, *t* test) and sustained (Fig. 1N; *t*₍₁₄₎ = 6.97, *p* < 0.0001, *t* test) components were attenuated in *Hcn1*^{M294L} mice compared with *WT* controls. Figure 2 shows that in *Hcn1*^{M294L} mice the OFF component was more attenuated (Fig. 2B–D) and was faster (Fig. 2E–G) in comparison with the ON component.

Given previous reports of color vision difficulties in human HCN1 DEE (McKenzie et al., 2022), we sought to examine responses elicited by colored stimuli to identify the potential functional absence of photoreceptors. Additionally, we assessed the temporal characteristics of *Hcn1*^{M294L} retinal responses using full-field flickering stimuli. Figure 3A shows that waveforms elicited using 10 Hz flickering stimuli of various peak colors were smaller in *Hcn1*^{M294L} mice compared with *Hcn1*^{WT} mice. Responses to

various colored stimuli were smaller in *Hcn1*^{M294L} mice (Fig. 3B; interaction *F*_(1,112) = 490.0, *p* < 0.0001, RM-ANOVA), particularly for 420–600 nm stimuli (Sidak multiple-comparisons test, *p* < 0.01). However, when normalized to the maximal amplitude, the spectral response function was similar between the two groups (Fig. 3C). Response amplitudes for flicker rates from 5 to 45 Hz differed between *Hcn1*^{M294L} and *Hcn1*^{WT} mice (Fig. 3D; interaction: *F*_(1,126) = 107.0, *p* < 0.001, RM-ANOVA), and *post hoc* comparison between groups identified significant attenuation in *Hcn1*^{M294L} mice for frequencies from 5 to 20 Hz (Sidak multiple-comparisons test, *p* < 0.05).

Retinal structure was assessed using *in vivo* optical coherence tomography imaging (Fig. 4A). There was no significant difference in layer thickness between *Hcn1*^{M294L} and *Hcn1*^{WT} mice, as follows: RNFL (Fig. 4B: *t*₍₁₈₎ = 0.067, *p* = 0.95, *t* test); GCL (Fig. 4C: *t*₍₁₈₎ = 1.79, *p* = 0.09, *t* test); IPL (Fig. 4D: *t*₍₁₈₎ = 1.08, *p* = 0.29,

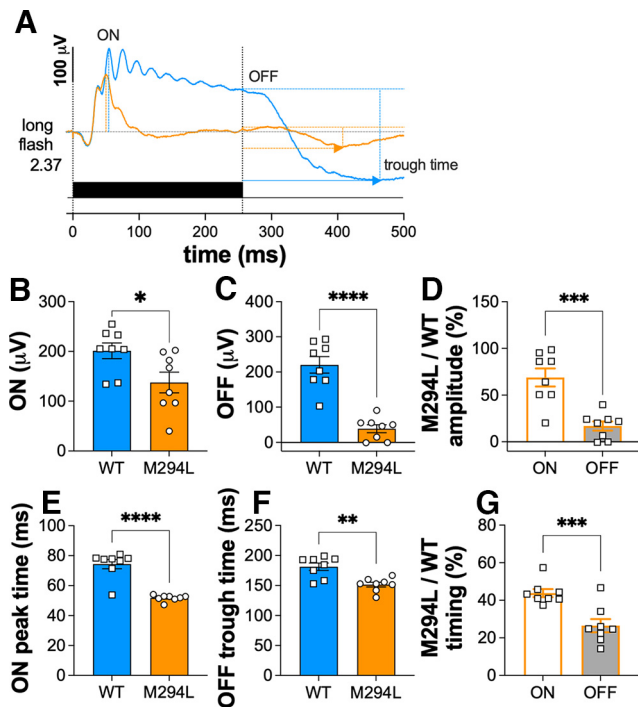


Figure 2. Comparison of ON and OFF electroretinogram responses in $Hcn1^{M294L}$ mice. **A**, A longer flash (256 ms) was used to elicit the murine ERG response from ON and OFF components. Amplitudes and implicit times were taken after light onset, as well as following light offset. OFF amplitudes were taken as the difference between the amplitudes at light offset (256 ms) and the OFF trough; also, the implicit time of the OFF trough. **B**, Group-averaged $Hcn1^{WT}$ mice (WT, $n = 8$, blue) and $Hcn1^{M294L}$ mice (M294L, $n = 8$, orange) ON amplitude ($t_{(14)} = 2.5$, $p = 0.03$). **C**, OFF amplitude ($t_{(14)} = 6.9$, $p < 0.0001$). **D**, Amplitudes of ON and OFF components are compared by expressing the amplitudes in $Hcn1^{M294L}$ mice relative to $Hcn1^{WT}$ mice ($t_{(14)} = 4.8$, $p = 0.0003$). **E**, ON-peak time ($t_{(14)} = 7.1$, $p < 0.0001$). **F**, OFF-trough time ($t_{(14)} = 4.1$, $p = 0.0012$). **G**, Implicit times of ON and OFF components are compared by expressing implicit time for $Hcn1^{M294L}$ mice relative to $Hcn1^{WT}$ mice ($t_{(14)} = 4.2$, $p = 0.0009$). * $p < 0.05$; ** $p < 0.01$; *** $p < 0.001$; **** $p < 0.0001$.

t test); INL (Fig. 4E: $t_{(18)} = 0.95$, $p = 0.36$, t test); OPL (Fig. 4F: $t_{(18)} = 1.60$, $p = 0.13$, t test); ONL (Fig. 4G: $t_{(18)} = 1.36$, $p = 0.19$, t test); PR (Fig. 4H: $t_{(18)} = 0.43$, $p = 0.67$, t test); and TRT (Fig. 4I: $t_{(18)} = 1.46$, $p = 0.16$, t test).

Immunohistochemistry showed that there were no gross retinal abnormalities in the $Hcn1^{M294L}$ mouse retina (Fig. 4M–O) compared with $Hcn1^{WT}$ mice (Fig. 4J–L) and no difference in the HCN1 channel location, which is highly expressed in the photoreceptors as well as in the outer and inner plexiform layers.

ERG responses in a female patient with HCN1 DEE

Table 2 compares the available parameters for the right and left eyes with normal data (Bradshaw et al., 2004; Meredith et al., 2004) collected using similar stimulus settings and electrodes (Kriss et al., 1992; Kriss and Russell-Eggitt, 1992; Kriss, 1994; Bradshaw et al., 2004; Marmoy et al., 2022). While the available normative ranges are for slightly older children (4–14 years), previous studies have suggested that the major ERG components are similar in amplitude and implicit time to adult ERGs by 6–10 months of age (Fulton et al., 1989). This comparison suggests that ERG responses for the patient fall below the most conservative 95% confidence limit for b-wave amplitude and timing, as well as for 30 Hz flicker amplitude. While the implicit time of the a-wave in the left eye was delayed, this was not the case for the right eye. The mouse ERG data reported above broadly recapitulate these clinical observations.

Computer simulation modeling of the photoreceptor responses

To gain further insight into the cellular mechanism underlying the altered ERG response observed for $Hcn1^{M294L}$ mice, we performed simulations using a model for a single photoreceptor. The model was based on previous studies (see Materials and Methods) and incorporated a leak, the nonspecific potassium conductance, and an L-type calcium conductance as well as a hyperpolarization-activated (I_h) component. For the I_h -related conductance, we used a 10-state allosteric model (Altomare et al., 2001; Hung et al., 2021) to predict the channel open probability. This was reduced to a four-state model to account for the altered kinetics of $Hcn1^{M294L}$ channels. We adjusted the original parameter set in Hung et al. (2021) to account for the faster mouse kinetics using brain slice voltage-clamp data as a template (Bleakley et al., 2021). As shown in Figure 5 (Table 1) under simulated voltage-clamp conditions, the hyperpolarization-activated current for $Hcn1^{M294L}$ mice shows a time-dependent activation component superimposed on an instantaneous current step, as we have previously described (Bleakley et al., 2021; Hung et al., 2021). The steady-state current–voltage relationships (Fig. 5C) from these data underscored the leaky behavior of $Hcn1^{M294L}$ channels and lacked the inward rectification characteristic of $Hcn1^{WT}$ channels over the physiologically relevant voltage range. The effect of HCN1 channels on simulated photoreceptor membrane potential is illustrated in Figure 5D. We assumed equal HCN1 maximum conductance for the WT and M294L cases. This was based on similar immunohistochemical expression patterns in the retina (Fig. 4) and similar maximal currents measured in layer 5 pyramidal neurons (Bleakley et al., 2021).

Under dark-adapted conditions preceding the flash, $Hcn1^{WT}$ and $Hcn1^{M294L}$ channels would not contribute significantly to the net membrane conductance as the predicted membrane potentials were -28 mV ($Hcn1^{WT}$) and -32 mV ($Hcn1^{M294L}$), respectively: $Hcn1^{WT}$ channels would be closed, whereas for $Hcn1^{M294L}$ channels, the predicted V_m corresponds to their reversal potential (Fig. 5B,D). With $Hcn1^{WT}$ in the model, the flash induced an instantaneous hyperpolarization, and as $Hcn1^{WT}$ channel-activated hyperpolarization was suppressed throughout the time course of the simulated photocurrent, giving rise to a pronounced “nose” in the V_m response (Barrow and Wu, 2009; Della Santina et al., 2010). In contrast, for $Hcn1^{M294L}$, hyperpolarization was significantly weaker during the flash and flatter in the subsequent plateau phase as the mutant channels conduct a larger inward current (Fig. 5D). As a consequence of the effect of HCN1 channel activity in shaping the time course of V_m , the corresponding time course of the L-type Ca current (I_{Ca}) was also affected (Fig. 5F). At the flash onset, our model predicted that I_{Ca} was fully suppressed for $Hcn1^{WT}$ as V_m would be sufficiently hyperpolarized to close these channels and subsequently they only begin to open toward the end of the simulated photoreceptor current time course as V_m recovers. In contrast, for the $Hcn1^{M294L}$, our simulations predicted only partial suppression of I_{Ca} at flash onset with an inward I_{Ca} of ~ 0.7 pA during the same period. We expect that the presence of a small, standing I_{Ca} during and following a bright-flash I_{Ca} would have consequences for the suppression of glutamate release at the synapse between photoreceptor and bipolar cells.

Discussion

In this study, we show that an *HCN1* pathogenic variant has a significant impact on retinal function. Most significantly, photoreceptor responses under both scotopic and photopic conditions were

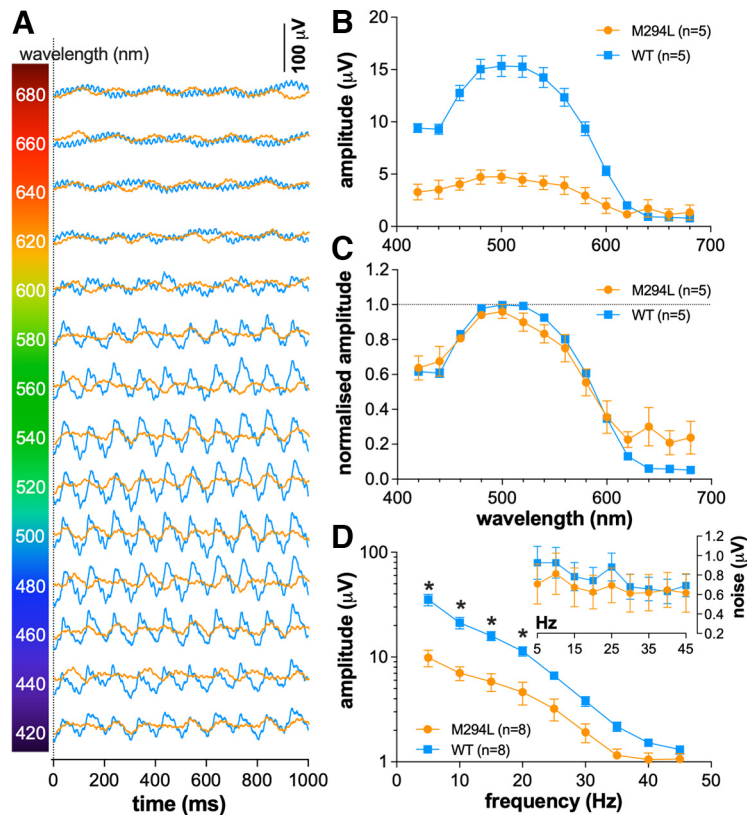


Figure 3. Deficits in temporal responses in *Hcn1*^{M294L} mice. **A**, Representative *Hcn1*^{WT} mice (WT, blue) and *Hcn1*^{M294L} mice (M294L, orange) waveforms at all wavelengths tested. **B**, Group average (\pm SEM) response to stimuli of different colors for *Hcn1*^{WT} mice ($n=5$, blue) and *Hcn1*^{M294L} mice ($n=5$, orange). **C**, Normalized spectral response functions for *Hcn1*^{WT} mice ($n=5$, blue) and *Hcn1*^{M294L} mice ($n=5$, orange). **D**, Group average (\pm SEM) responses for *Hcn1*^{WT} mice ($n=8$, blue) and *Hcn1*^{M294L} mice ($n=8$, orange) as a function of flicker frequency. * $p < 0.05$ post hoc test between groups. Quantification of noise amplitude at 50 Hz for all flicker frequencies can be found in the inset. Group average (\pm SD) noise amplitude obtained from spectral analysis of the ERG signal at 50 Hz in *Hcn1*^{WT} (WT, $n=8$, blue) and *Hcn1*^{M294L} mice (M294L, $n=8$, orange) collected across the range of temporal frequencies used. Two-way repeated-measures ANOVA showed that there was no statistically significant interaction between genotype and frequency ($F_{(1,8)} = 0.09$, $p = 0.99$) or a difference in genotype ($F_{(1,8)} = 1.65$, $p = 0.19$) or frequency ($F_{(1,8)} = 0.54$, $p = 0.83$).

significantly less sensitive to light. Furthermore, postphotoreceptor responses were smaller, less sensitive to light and showed an impaired capacity to resolve stimuli of high temporal frequency. These mouse results are in line with ERG recordings from a patient with HCN DEE because of the *HCN1* M305L pathogenic variant. Visual deficits driven by retinal dysfunction are therefore highly likely to be a feature of *HCN1* DEE caused by pathogenic variants, resulting in cation leak.

HCN1 channels are abundantly expressed in rod and cone photoreceptor inner segments (Müller et al., 2003; Ivanova and Müller, 2006; Della Santina et al., 2010) and are activated after a short delay to drive the membrane potential back to the resting state (Knop et al., 2008; Della Santina et al., 2010; Seeliger et al., 2011). This makes the photoreceptor response faster, creating the characteristic nose profile (Barrow and Wu, 2009; Della Santina et al., 2012). Previous studies show that HCN1 channel knockout (KO) does not affect the ERG a-wave and only manifests as a prolongation of the b-wave in mice (Seeliger et al., 2011; Sothilingam et al., 2016). This is consistent with the fact that HCN1 channels are only open after light has closed cyclic nucleotide-gated channels (Moosmang et al., 2001; Demontis et al., 2002; Knop et al., 2008; Tanimoto et al., 2012). As such, HCN1 channels are not expected to affect the a-wave

or light sensitivity (Della Santina et al., 2012). However, we show here that the *Hcn1*^{M294L} variant causes a reduced a-wave sensitivity to light as well as a downstream reduction in b-wave sensitivity to light. A key difference between *Hcn1* knock-out and *Hcn1*^{M294L} knock-in mice is that the knock-in missense variant would impact cellular excitability. By being constitutively open, abnormal inward cation flux through the mutant channels is likely to impact passive cell properties. This idea is supported by previous reports that constitutively open HCN1 channels cause a significant change in resting membrane potential in cortical and hippocampal neurons (Bleakley et al., 2021). Furthermore, a standing “cation leak” will shape light-induced changes in membrane potential. Consistent with this, our computer simulations (Fig. 5D) suggest that light-induced hyperpolarization was weaker at flash onset because of the presence of a standing leak conductance. Our simulations also indicate that following the initial hyperpolarization, V_m shows a flatter plateau phase (less prominent nose) as the mutant channels conduct a larger inward current at these voltages when compared with WT channels, and the time-dependent activation component constitutes a smaller proportion of total I_h (Fig. 5D,E). Reduced light-induced hyperpolarization along with impaired shaping of the photoreceptor response might account for slower scotopic (Fig. 1C) and photopic (Fig. 1J) a-wave responses (i.e., less sensitivity to light).

Our simulations show that in the complete absence of HCN1, light-induced hyperpolarization is larger, but has a flatter plateau phase. This is consistent with patch-clamp photoreceptor recordings from *Hcn1*^{-/-} as well as *Hcn1*^{WT} mice in the presence of the channel blocker ivabradine (Della Santina et al., 2012). A similar flatter plateau phase is also described for the *HCN1* pathogenic variant, a consequence of the significantly attenuated voltage dependence of the channels. The lack of this dynamic change in V_m during a light stimulus may account for the fact that deficits in temporal processing are seen in both the mutant and knock-out cases (Seeliger et al., 2011; Sothilingam et al., 2016).

Seeliger et al. (2011) show in *Hcn1*^{-/-} mice that if the rods are silenced, then cone responses improve. Thus, at mesopic light levels HCN1 channels on rods influence the cone response (Lankford et al., 2022). Here we show, using photopic conditions, which saturate rod photoreceptors, that there is a robust deficit in cone-mediated responses both in response to short flashes as well as with high temporal frequency flickering stimuli. This shows that in the *Hcn1*^{M294L} mouse HCN1 channels on both rod and cone receptors are impacted. Indeed, by fitting the a-wave leading edge, we found that the reduction in light sensitivity was greater in the photopic ERG compared with the scotopic mixed response (-0.23 ± 0.05 vs -0.08 ± 0.03 log units, $t_{(14)} = 2.39$, $p = 0.03$, t test).

Our simulation modeling suggests that light-induced changes in Ca^{2+} concentration in the simulated rod response is reduced,

which will result in the glutamate release during a light flash being attenuated, potentially explaining the downstream reduction of the bipolar b-wave amplitude and sensitivity under scotopic conditions and the reduced sensitivity under photopic conditions (Fig. 1*D,E,L*). It also is likely that the combination of slower and more prolonged photoreceptor responses (Fig. 4*E*) along with reduced glutamatergic neurotransmission between rod photoreceptors and bipolar cells accounts for the impairment of flicker fusion frequency in *Hcn1*^{M294L} mutant mice (Fig. 2). However, a differential effect of the mutation on ON and OFF responses, as observed in Figure 2, and as has been previously reported following ivabradine blockade of HCN1 channels (Bemme et al., 2017), may also contribute to the impairment of temporal responses in *Hcn1*^{M294L} mutant mice.

It is noteworthy that in *Hcn1*^{−/−} mice the rod b-wave is prolonged (Seeliger et al., 2011; Sothilingam et al., 2016), whereas in *Hcn1*^{M294L} mutant mice the ERG b-wave is more truncated, which is particularly apparent in the photopic ERG (Fig. 1*H*). Despite these difference in the single flash ERG, we observed reductions in the flicker fusion frequency (Fig. 3*B*) that are consistent with the deficit seen in *Hcn1*^{−/−} mice (Seeliger et al., 2011; Sothilingam et al., 2016). Based on our modeling, we speculate that in *Hcn1*^{−/−} mice a larger and more prolonged light-induced photoreceptor hyperpolarization produces a larger and more sustained b-wave. Furthermore, the absence of temporal shaping of photoreceptor response results in impaired temporal responses (reduced flicker fusion frequency). In the case of the *Hcn1*^{M294L} mutant mouse, a smaller light-induced hyperpolarization results in a smaller b-wave, and at the same time the loss of temporal shaping leads to the same flicker fusion deficit as in *Hcn1*^{−/−} mice.

Within the scotopic pathway, we also noted that the reduction in bipolar cell b-wave light sensitivity (-0.42 ± 0.25 log units) was much greater than would be predicted based on the attenuation of the a-wave sensitivity (-0.08 ± 0.09 log units) to light. Furthermore, the reduction in the ganglion cell-mediated pSTR amplitude is more than would be expected based on attenuation of bipolar cell b-wave amplitude. This raises the possibility that within the rod pathway abnormal HCN1 channel activity on inner retinal neurons may contribute to the phenotype. Specifically, HCN1 channels are also found on bipolar cells and are concentrated at synaptic terminals and play a role in modulating bipolar cell synaptic transmission (Chevalere and Castillo, 2002; Müller et al., 2003; Della Santina et al., 2010). This is true particularly for bipolar cells that show high temporal tuning (Euler et al., 2014) and

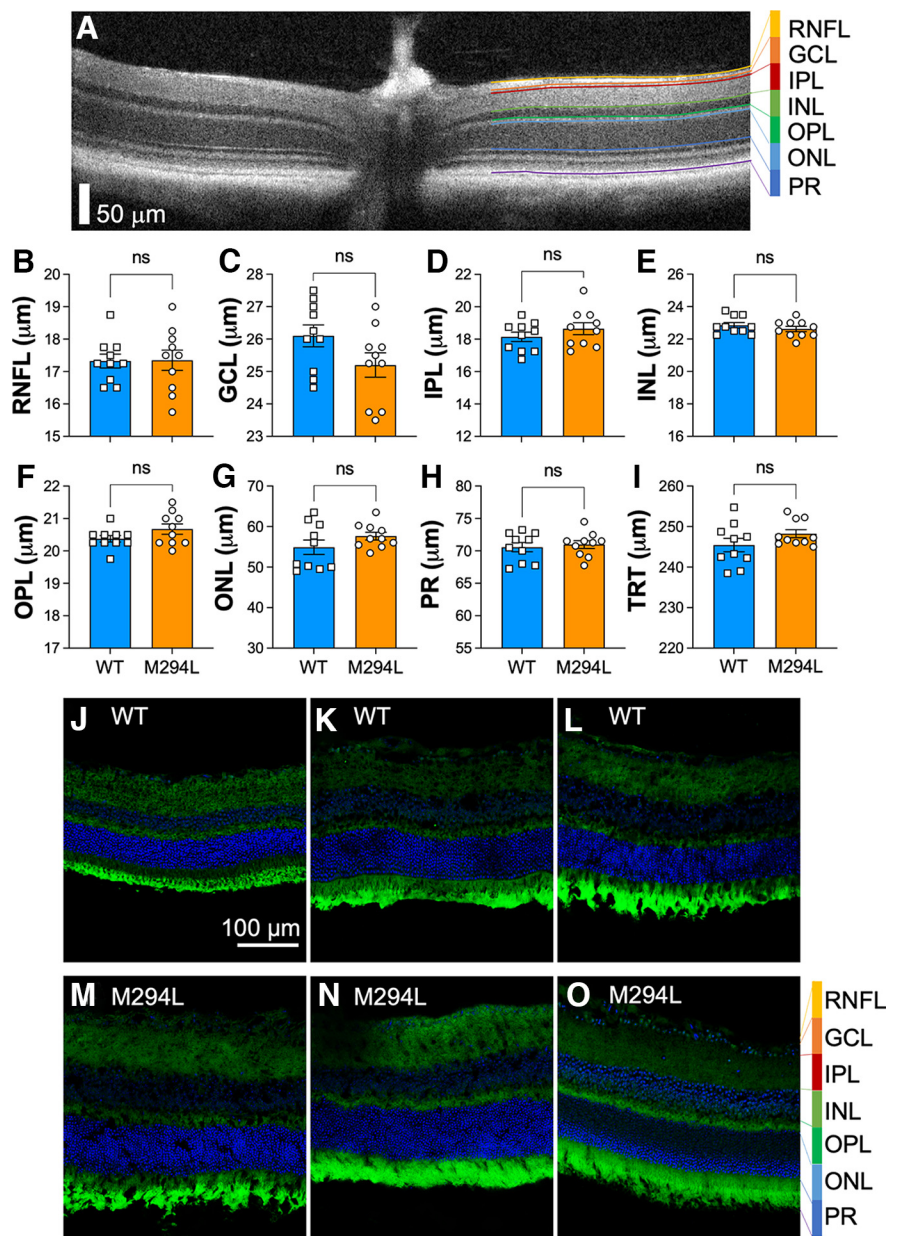


Figure 4. Normal gross retinal structure in *Hcn1*^{M294L} mice. **A**, Example of optical coherence tomography image of the mouse retina centered at the optic nerve, with the segmentation location of the retinal layers shown. **B**, Group averaged *Hcn1*^{WT} mice (WT, $n = 10$, blue) and *Hcn1*^{M294L} mice (M294L, $n = 10$, orange) RNFL thickness. **C**, Ganglion cell layer (GCL). **D**, inner plexiform layer (IPL). **E**, inner nuclear layer (INL). **F**, outer plexiform layer (OPL). **G**, outer nuclear layer (ONL). **H**, Photoreceptor (PR) thickness. **I**, total retinal thickness (TRT). **J–L**, Retinal cross section from *Hcn1*^{WT} mice stained for HCN1 channels (green) and counterstained for cell nuclei with DAPI (blue). **M–O**, Retinal cross sections from *Hcn1*^{M294L} mice. ns, Not significant.

contribute to motion detection pathways (Yonehara et al., 2013). Recently, Hellmer et al. (2020) show that HCN currents are important for shaping of subgroups of bipolar cells and that such current can be modulated by a range of receptors. Whether the deficit in temporal processing reflects change to photoreceptor as well as inner retinal HCN channels requires further investigation. Moreover, studies quantifying synaptic terminals mediating communication between photoreceptor and bipolar cells would be important to fully understand the nature of the functional deficits seen here. Furthermore, it may be likely that development and refinement of retinal circuitry is also impacted.

Table 2. Clinical data from a patient with HCN1 DEE compared with normal data collected using similar stimulus settings and skin electrodes

Waveform	Parameter	Mean/median (confidence limits)		
		Patient data	Bradshaw et al. (2004)	Meredith et al. (2004)
Notes		ISCEV Single flash cone 10 months old	ISCEV Single flash cone 4–14 years old	ISCEV Single flash cone 4–14 years old
a-wave	Amplitude (μV)		15 (12–17)	15 (5–25)
	Implicit time (ms)	RE 15, LE 16	13.9 (12.9–14.9)	14 (12.2–15.8)
b-wave	Amplitude (μV)	RE 23, LE 21.5	50 (42–63)	52 (24–80)
	Implicit time (ms)	RE 34, LE 33	30.8 (30.8–30.8)	30.9 (29.5–32.3)
30 Hz flicker	Amplitude (μV)	RE 18.8, LE 16.5	31 (25–34)	30 (20–40)

DDE, Developmental and epileptic encephalopathies; ISCEV, International Society for Clinical Electrophysiology of Vision; LE, left eye; RE, right eye.

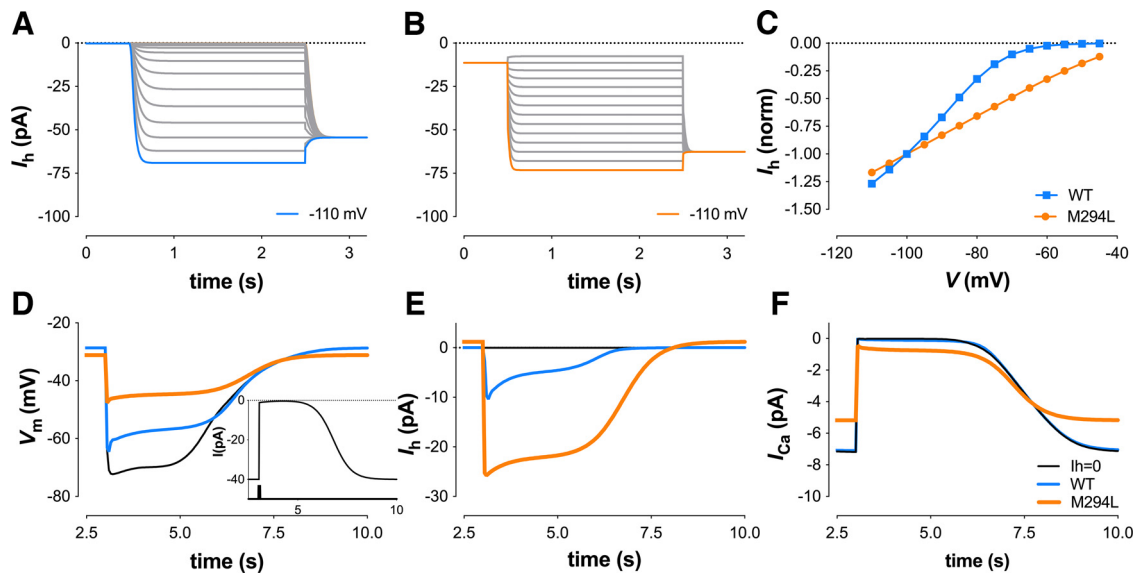


Figure 5. *A, B*, Simulated voltage-clamp records for $Hcn1^{WT}$ mice (*A*) and $Hcn1^{M294L}$ mice (*B*) showing HCN1-related current in response to a series of voltage steps from -110 to -45 mV in 5 mV intervals from a -50 mV holding potential and returning to -100 mV. The pulse to -110 mV has been highlighted for clarity. This pulse protocol matches that used in Bleakley et al. (2021, their Fig. 5A) from mouse brain slice whole-cell patch recordings. *C*, The corresponding steady-state current–voltage relationships normalized to -100 mV show a clear absence of inward rectification for M294L (orange) compared with the WT (blue). *D–F*, Simulated response of the generic photoreceptor to a bright flash (see text and inset) for membrane potential (V_m) for $Hcn1^{WT}$ mice (blue) and $Hcn1^{M294L}$ mice (orange) and in the absence of HCN1 (black); *D*), HCN-related current (I_h ; *E*), and voltage-dependent I_{Ca} (*F*) for WT (blue traces) and M294L (orange traces), and in the absence of HCN1 (black traces). Note the timescale offset to allow steady state to be reached before the flash onset. Details on modeling parameters can be found in Table 1.

The potential for developmental delays has been addressed through comprehensive characterization demonstrating that $Hcn1^{M294L}$ show clear behavioral deficits, some of which are indicative of developmental delays (Bleakley et al., 2021).

One may have expected a proportional decrease in the OPs, given the attenuation of photoreceptor and bipolar cell-mediated responses seen in the $Hcn1^{M294L}$ mutant mouse, as is the case in $Hcn1^{-/-}$ mice (Knop et al., 2008). However, the impact of HCN1 cation leak may vary depending on retinal location. For instance, HCN1 channels may modulate OPs via their expression in the IPL on ON–bipolar cell axon terminals, as well in the OFF layer of the IPL on amacrine cells (Müller et al., 2003; Knop et al., 2008). Furthermore, HCN channels can modulate GABAergic neurotransmission (Cai et al., 2022), which can impact bipolar cell response shaping. Should aberrant HCN channels modulate the balance of GABAergic signaling from amacrine to bipolar cells, this can lead to changes in OPs, and in some cases can lead to paradoxically larger OPs (Kapousta-Bruneau, 2000; McCall et al., 2002), despite upstream a-wave and b-wave attenuation.

The clinical ERG assessment of light-adapted response in a patient with the same $HCN1$ pathogenic variant, which leads to constitutively open HCN1 channels, shows a pattern of smaller b-wave and 30 Hz flicker responses, which is recapitulated in the $Hcn1^{M294L}$ mouse. While there has been a previous report of color vision deficits (McKenzie et al., 2022), this is the first report of reduced temporal processing in HCN1 DEE. Critically, these data indicate that individuals with a cation-leak $HCN1$ pathogenic variant are likely to have impaired vision, including reduced sensitivity to light and significant problems with processing visual stimuli of moderate to high temporal frequencies. Furthermore, altered dynamics of the Ca^{2+} concentration in photoreceptors is also likely to impact light adaptation (Chen et al., 2010). Such findings may have clinical implications for patients, given that our eyes are constantly sampling information of images projected onto the retina. Information gathered periodically is integrated so that objects around us appear to be stable or move smoothly. Thus, good temporal processing is important to all visual activities. Further understanding of the precise visual deficit will help clinicians to design visual environments that optimize visual function.

In summary, this is the first study to examine the visual impact of a pathogenic variant in *HCN1* that leads to a cation leak. Together, our data identify the impact of *HCN1* pathogenic variants on vision and provide further insights into the important role that HCN1 channels play. Finally, our study highlights the potential usefulness of clinical measures of comorbid states, such as visual dysfunction, which may provide useful biomarkers for monitoring and assessing treatment efficacy in relevant forms of epilepsy.

References

- Altomare C, Bucchi A, Camatini E, Baruscotti M, Viscomi C, Moroni A, DiFrancesco D (2001) Integrated allosteric model of voltage gating of HCN channels. *J Gen Physiol* 117:519–532.
- Barrow AJ, Wu SM (2009) Low-conductance HCN1 ion channels augment the frequency response of rod and cone photoreceptors. *J Neurosci* 29:5841–5853.
- Baylor DA, Matthews G, Nunn BJ (1984) Location and function of voltage-sensitive conductances in retinal rods of the salamander, *Ambystoma tigrinum*. *J Physiol* 354:203–223.
- Bemse S, Weick M, Gollisch T (2017) Differential effects of HCN channel block on on and off pathways in the retina as a potential cause for medication-induced phosphene perception. *Invest Ophthalmol Vis Sci* 58:4754–4767.
- Biel M, Wahl-Schott C, Michalakis S, Zong X (2009) Hyperpolarization-activated cation channels: from genes to function. *Physiol Rev* 89:847–885.
- Bleakley LE, McKenzie CE, Soh MS, Forster IC, Pinares-Garcia P, Sedo A, Kathirvel A, Churilov L, Jancovski N, Maljevic S, Berkovic SF, Scheffer IE, Petrou S, Santoro B, Reid CA (2021) Cation leak underlies neuronal excitability in an HCN1 developmental and epileptic encephalopathy. *Brain* 144:2060–2073.
- Bonzanni M, DiFrancesco JC, Milanese R, Camprostrini G, Castellotti B, Bucchi A, Baruscotti M, Ferrarese C, Franceschetti S, Canafoglia L, Ragona F, Freri E, Labate A, Gambardella A, Costa C, Rivolta I, Gellera C, Granata T, Barbuti A, DiFrancesco D (2018) A novel de novo HCN1 loss-of-function mutation in genetic generalized epilepsy causing increased neuronal excitability. *Neurobiol Dis* 118:55–63.
- Bradshaw K, Hansen R, Fulton A (2004) Comparison of ERGs recorded with skin and corneal-contact electrodes in normal children and adults. *Doc Ophthalmol* 109:43–55.
- Bui BV, Fortune B (2004) Ganglion cell contributions to the rat full-field electroretinogram. *J Physiol* 555:153–173.
- Bui BV, Edmunds B, Cioffi GA, Fortune B (2005) The gradient of retinal functional changes during acute intraocular pressure elevation. *Invest Ophthalmol Vis Sci* 46:202–213.
- Cai W, Liu SS, Li BM, Zhang XH (2022) Presynaptic HCN channels constrain GABAergic synaptic transmission in pyramidal cells of the medial prefrontal cortex. *Biol Open* 11:bio058840.
- Chen J, Woodruff ML, Wang T, Concepcion FA, Tranchina D, Fain GL (2010) Channel modulation and the mechanism of light adaptation in mouse rods. *J Neurosci* 30:16232–16240.
- Chevalerey V, Castillo PE (2002) Assessing the role of Ih channels in synaptic transmission and mossy fiber LTP. *Proc Natl Acad Sci U S A* 99:9538–9543.
- Della Santina L, Bouly M, Asta A, Demontis GC, Cervetto L, Gargini C (2010) Effect of HCN channel inhibition on retinal morphology and function in normal and dystrophic rodents. *Invest Ophthalmol Vis Sci* 51:1016–1023.
- Della Santina L, Piano I, Cangiano L, Caputo A, Ludwig A, Cervetto L, Gargini C (2012) Processing of retinal signals in normal and HCN deficient mice. *PLoS One* 7:e29812.
- Demontis GC, Moroni A, Gravante B, Altomare C, Longoni B, Cervetto L, DiFrancesco D (2002) Functional characterisation and subcellular localisation of HCN1 channels in rabbit retinal rod photoreceptors. *J Physiol* 542:89–97.
- Euler T, Haverkamp S, Schubert T, Baden T (2014) Retinal bipolar cells: elementary building blocks of vision. *Nat Rev Neurosci* 15:507–519.
- Fulton AB, Hartmann EE, Hansen RM (1989) Electrophysiologic testing techniques for children. *Doc Ophthalmol* 71:341–354.
- Hellmer CB, Bohl JM, Hall LM, Koehler CC, Ichinose T (2020) Dopaminergic modulation of signal processing in a subset of retinal bipolar cells. *Front Cell Neurosci* 14:253.
- Hestrin S (1987) The properties and function of inward rectification in rod photoreceptors of the tiger salamander. *J Physiol* 390:319–333.
- Hung A, Forster IC, McKenzie CE, Berecki G, Petrou S, Kathirvel A, Soh MS, Reid CA (2021) Biophysical analysis of an HCN1 epilepsy variant suggests a critical role for S5 helix Met-305 in voltage sensor to pore domain coupling. *Prog Biophys Mol Biol* 166:156–172.
- Ivanova E, Müller F (2006) Retinal bipolar cell types differ in their inventory of ion channels. *Vis Neurosci* 23:143–154.
- Kamiyama Y, Ogura T, Usui S (1996) Ionic current model of the vertebrate rod photoreceptor. *Vision Res* 36:4059–4068.
- Kapousta-Bruneau NV (2000) Opposite effects of GABA(A) and GABA(C) receptor antagonists on the b-wave of ERG recorded from the isolated rat retina. *Vision Res* 40:1653–1665.
- Knop GC, Seeliger MW, Thiel F, Mataruga A, Kaupp UB, Friedburg C, Tanimoto N, Müller F (2008) Light responses in the mouse retina are prolonged upon targeted deletion of the HCN1 channel gene. *Eur J Neurosci* 28:2221–2230.
- Kriss A (1994) Skin ERGs: their effectiveness in paediatric visual assessment, confounding factors, and comparison with ERGs recorded using various types of corneal electrode. *Int J Psychophysiol* 16:137–146.
- Kriss A, Russell-Eggitt I (1992) Electrophysiological assessment of visual pathway function in infants. *Eye* 6:145–153.
- Kriss A, Jeffrey B, Taylor D (1992) The electroretinogram in infants and young children. *J Clin Neurophysiol* 9:373–393.
- Lamb TD, Pugh ENJ (1992) A quantitative account of the activation steps involved in phototransduction in amphibian photoreceptors. *J Physiol* 449:719–758.
- Lankford CK, Umino Y, Poria D, Kefalov V, Solessio E, Baker SA (2022) Cone-driven retinal responses are shaped by rod but not cone HCN1. *J Neurosci* 42:4231–4249.
- Liu XD, Kourennyi DE (2004) Linear system analysis of ion channel modulation in rod photoreceptors under dim light conditions. *Conf Proc IEEE Eng Med Biol Soc* 2004:4037–4040.
- Marini C, et al. (2018) HCN1 mutation spectrum: from neonatal epileptic encephalopathy to benign generalized epilepsy and beyond. *Brain* 141:3160–3178.
- Marmoy OR, Moinuddin M, Thompson DA (2022) An alternative electroretinography protocol for children: a study of diagnostic agreement and accuracy relative to ISCEV standard electroretinograms. *Acta Ophthalmol* 100:322–330.
- McCall MA, Lukasiewicz PD, Gregg RG, Peachey NS (2002) Elimination of the rho1 subunit abolishes GABA(C) receptor expression and alters visual processing in the mouse retina. *J Neurosci* 22:4163–4174.
- McKenzie CE, Ho CJ, Forster IC, Soh MS, Phillips AM, Chang YC, Scheffer IE, Reid CA, Tsai MH (2022) Impaired color recognition in HCN1 epilepsy: a single case report. *Front Neurol* 13:834252.
- Meredith SP, Reddy MA, Allen LE, Moore AT, Bradshaw K (2004) Full-field ERG responses recorded with skin electrodes in paediatric patients with retinal dystrophy. *Doc Ophthalmol* 109:57–66.
- Moosmang S, Stieber J, Zong X, Biel M, Hofmann F, Ludwig A (2001) Cellular expression and functional characterization of four hyperpolarization-activated pacemaker channels in cardiac and neuronal tissues. *Eur J Biochem* 268:1646–1652.
- Müller F, Scholten A, Ivanova E, Haverkamp S, Kremmer E, Kaupp UB (2003) HCN channels are expressed differentially in retinal bipolar cells and concentrated at synaptic terminals. *Eur J Neurosci* 17:2084–2096.
- Nava C, et al. (2014) De novo mutations in HCN1 cause early infantile epileptic encephalopathy. *Nat Genet* 46:640–645.
- Porro A, Abbondato G, Veronesi V, Russo A, Binda A, Antolini L, Granata T, Castellotti B, Marini C, Moroni A, DiFrancesco JC, Rivolta I (2021) Do the functional properties of HCN1 mutants correlate with the clinical features in epileptic patients? *Prog Biophys Mol Biol* 166:147–155.

- Publio R, Oliveira RF, Roque AC (2006) A realistic model of rod photoreceptor for use in a retina network model. *Neurocomputing* 69:1020–1024.
- Saszik SM, Robson JG, Frishman LJ (2002) The scotopic threshold response of the dark-adapted electroretinogram of the mouse. *J Physiol* 543:899–916.
- Seeliger MW, Brombas A, Weiler R, Humphries P, Knop G, Tanimoto N, Müller F (2011) Modulation of rod photoreceptor output by HCN1 channels is essential for regular mesopic cone vision. *Nat Commun* 2:532.
- Sothilingam V, Michalakis S, Garcia Garrido M, Biel M, Tanimoto N, Seeliger MW (2016) HCN1 channels enhance rod system responsivity in the retina under conditions of light exposure. *PLoS One* 11:e0147728.
- Tanimoto N, Brombas A, Müller F, Seeliger MW (2012) HCN1 channels significantly shape retinal photoresponses. *Adv Exp Med Biol* 723:807–812.
- Wachtmeister L (1998) Oscillatory potentials in the retina: what do they reveal. *Prog Retin Eye Res* 17:485–521.
- Yonehara K, Farrow K, Ghanem A, Hillier D, Balint K, Teixeira M, Jüttner J, Noda M, Neve RL, Conzelmann KK, Roska B (2013) The first stage of cardinal direction selectivity is localized to the dendrites of retinal ganglion cells. *Neuron* 79:1078–1085.